UCLA
UCLA Electronic Theses and Dissertations

Title

Hydride Formation Modeling and Ethanol Dehydrogenation Simulation in Transition Metal Catalyst Systems

Permalink

https://escholarship.org/uc/item/9fx9v581

Author

Liu, Xihan

Publication Date

2023

Peer reviewed|Thesis/dissertation

UNIVERSITY OF CALIFORNIA

Los Angeles

Hydride Formation Modeling and Ethanol Dehydrogenation

Simulation in Transition Metal Catalyst Systems

A thesis submitted in partial satisfaction

of the requirements for the degree

Master of Science in Chemical Engineering

by

Xihan Liu

2023

ABSTRACT OF THE THESIS

Hydride Formation Modeling and Ethanol Dehydrogenation
Simulation in Transition Metal Catalyst Systems

by

Xihan Liu

Master of Science in Chemical Engineering

University of California, Los Angeles, 2023

Professor Philippe Sautet, Chair

DFT-based simulations of hydride formation in the Pd/Au systems probe the thermodynamic insight of this process. The hydride formation in the 1 ML and 2 ML Pd structures was found unfavorable, with the free energies of formation being positive under the experimental conditions of interest. Nonetheless, the formation energy was reduced as the hydrogen content increased, proving the stabilization effect of hydrogen atoms. DFT calculations also revealed that the hydrogen atoms would occupy the surface sites first in the case where surface and subsurface sites were both available. The reaction pathway of EtOH dehydrogenation was investigated theoretically using DFT calculations. The rate-limiting step of the overall reaction was found to be the O-H bond cleavage step. By surveying different transition states of each bond cleavage step, the overall reaction would go through an O-H bond scission process, followed by a C-H bond scission process, to have the smallest overall barrier. However, more kinetic details of the reaction would require further microkinetic simulations.

The thesis of Xihan Liu is approved.

Dante A. Simonetti

Panagiotis D. Christofides

Philippe Sautet, Committee Chair

University of California, Los Angeles

2023

TABLE OF CONTENTS

LIST OF FIGURES

LIST OF TABLES

ACKNOWLEDGMENTS

First and most importantly, I would like to thank my thesis advisor, Professor Philippe Sautet, who constantly offers help and guidance to me. He is one of the most knowledgeable scholars I have met at UCLA, yet a very modest and caring researcher.

Also, I would like to express my gratitude to current and former members of Professor Sautet's group, particularly Michael Ngan, David Lim, and George Yan. Additionally, I truly acknowledge Professor Christofides and Professor Simonetti who serve on my thesis committee and provide great insights into my thesis.

Besides, I would like to thank my parents who give me enduring support. I would not have achieved my academic goal without their help. I also have to say thank you to my friends at UCLA and in China.

Finally, I sincerely appreciate the support from the University of California, Los Angeles, specifically the UCLA Institute for Digital Research and Education (IDRE) and the computational resources on the Hoffman2 cluster. I also thank the computational resources on the Bridges2 cluster from the ACCESS program.

This thesis contains materials from unpublished manuscripts in Chapters 1 to 5.

CHAPTER 1

Introduction

1.1 Heterogeneous Catalysis

The most important aspect of studying catalysis is to promote the sustainability and efficiency of chemical production, and this will facilitate the realization of green chemistry in industrial productions [1]. Additional benefits include considerable selectivity in catalytic reactions, allowing the reactions to take place in the desired directions. The three major factors in industrial catalyst designs are activity/selectivity, catalyst life cycle, and fluid dynamic properties, as shown in Figure 1.1 [1]. Currently, catalysts, specifically zeolites and metal oxides, are heavily used in the petroleum industry to expedite the hydroprocessing of heavy oils [2]. Studies have shown extraordinary advantages of using zeolites in the petroleum refining processes for better coke selectivity, higher activity, and more stable structure [3]. Besides, the production of ammonia, also known as the Haber-Bosch process, also heavily relies on catalysis. The details of this reaction are shown in Figure 1.2 [4]. The catalysts used in this process have evolved and expanded into different categories, from the iron oxide-based catalysts initially, to the later innovated ruthenium-based catalysts, and currently, researchers are trying to apply photocatalysis to this reaction despite several challenges, such as low efficiency [4]. Nowadays, one of the most cutting-edge applications of catalysts is the carbon dioxide (CO_2) capture. This application can help offset the negative effects of the recent surge of CO_2 emissions from the transportation and chemical production sectors. Metal-organic frameworks (MOFs) have been extensively investigated and utilized in the CO_2 capture process, and they have versatile ways of construction, expanding their

1

usage in numerous industrial processes [5].
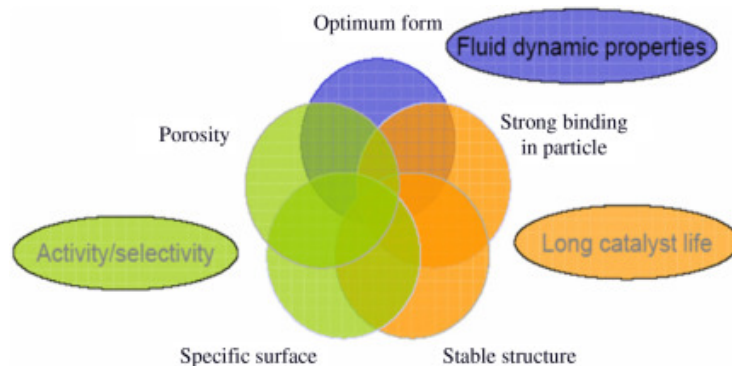
Figure 1.1: The main factors of industrial catalyst design (figure extracted from J. C. Védrine's work [1]).
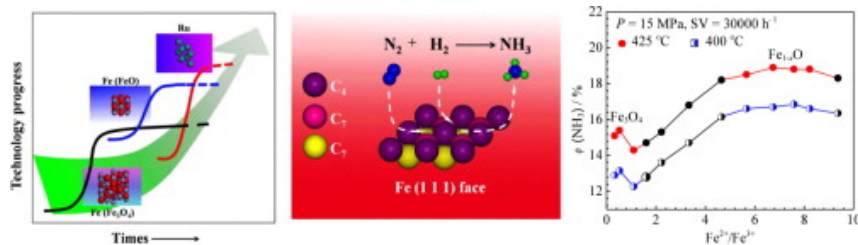
Figure 1.2: The development and reaction details of the Haber-Bosch process (figure extracted from H. Liu's work [4]).

With the advancement of computational power in the modern society, theoretical studies on heterogeneous catalysts become more accurate and fast, yet precise simulations of real catalysts remain arduous due to their intrinsic nature of complexity. A multi-scale modeling is often required to carry out, deriving the insights of a single aspect at a time, as there is a lack of a comprehensive and well-developed technique that can acquire the information of all perspectives needed to depict the overall reaction [6]. Figure 1.3 below describes the common scheme for multi-scale models. The first step in the scheme is the density functional theory (DFT) calculations on the electronic structure, providing mechanistic details of chemical reactions. This step usually involves geometry optimizations and transition state calculations.

The second step involves microkinetic models, where the important kinetic information will be extracted. In the end, the macroscopic transport phenomena that will take place in the actual reactor, heat and mass transfers particularly, will be modeled [6].
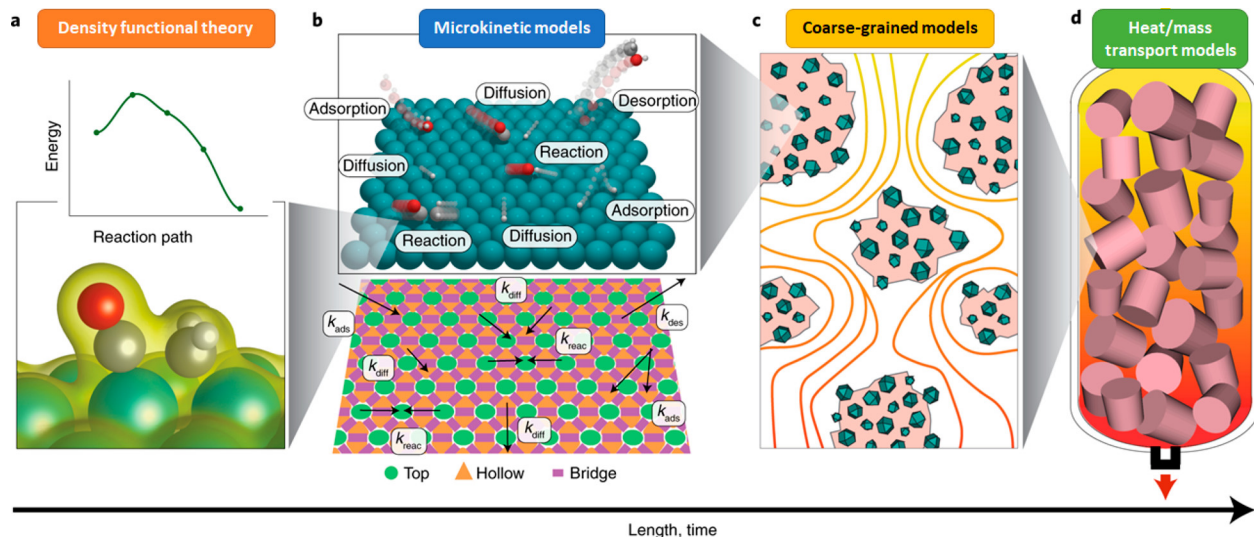
Figure 1.3: The scheme of a multi-scale simulation (figure extracted from B. W. J. Chen et al's work [6]).

1.2   Palladium Hydride (PdH$_x$)

Palladium metal has drawn people's attention in the field of catalytic hydrogenation reactions for the past few decades due to its pronounced selectivity and activity [7]. Gaseous hydrogen molecules can dissociate on Pd surfaces and easily diffuse into the subsurface layer to form hydride; furthermore, because of this nature, there are some potential applications, for example, hydrogen storage devices, separation membranes, and more viably hydrogenation reaction catalysts [8]. Since hydride can be easily formed in Pd structures during hydrogenation reactions, studying the thermodynamic and kinetic properties of hydride formation is the key to understanding the role of hydride in these reactions. Palladium hydride (PdH$_x$) is now hypothesized to play a significant part in determining the selectivity and reactivity

in hydrogenation reactions.

Previous studies proved that hydrogen adsorption had stabilization effects on Pd(111) surface. The adsorption energy per hydrogen atom was lower at high hydrogen content than that at low hydrogen content [9]. This indicates that the surface can be stabilized by introducing hydrogen atoms. Besides, hydrogen in both the α and β phase would coexist on the pure Pd nanoparticles, and this could lead to hysteresis, and commonly, to enhance the reaction kinetics and ameliorate the hysteresis effect, we combine Pd with other alloying metals, such as Au [10]. Typically, the two phases vary in the hydrogen concentration and fcc lattice constant. The α phase has a lower hydrogen concentration and a smaller fcc lattice constant while the β phase has a higher hydrogen concentration and a greater fcc lattice constant [9].

1.3   Ethanol Dehydrogentaion

Previous work has shown that single-atom alloys (SAAs) exhibited assuring potential in performing dehydrogenation reactions. Because of their good activity and selectivity, they have been studied extensively over the past few years [11]. However, rational designs of heterogeneous catalysts still remain complicated. Specifically for ethanol (EtOH) dehydrogenation reactions, several catalysts have been exhaustively studied using experimental and computational approaches [12–14]. Previous studies revealed that single-atom alloy (SAA) catalysts, specifically nickel copper (NiCu), were very promising. Aldehyde formation was observed below 150 ^{o}C, and this can be attributed to the atomic dispersion, which drastically decreases the activation barrier of the C-H bond [15]. The other previous work showed that Cu(111) and Cu(110) surfaces exhibited good selectivity but poor activity in this type of reaction. A good way to improve the activity was to add another metal in a small amount to the Cu surface to form SAA [16]. The Ni monomer on the Cu(111) surface (NiCu) has been studied previously as a good catalyst for various reactions while the Ni dimer on the

Cu(111) surface (Ni$_2$Cu) has attracted people's eyes for its even better catalytic performance [17].

The most important motivation for ethanol dehydrogenation is to produce hydrogen gas (H$_2$) in a more environment-friendly and sustainable way. H$_2$ is an essential molecule in the industry nowadays. Currently, the vast majority of H$_2$ is produced through methane reforming, which heavily relies on fossil fuel combustion. This potentially results in excessive carbon dioxide (CO$_2$) emission, aggravating global warming effects, and overusing nonrenewable natural resources [18]. Aldehyde, the other product of EtOH hydrogenation, is also widely used as a chemical precursor for a variety of compounds, for example, acetic acid [19]. Theoretical and experimental investigations on catalytic EtOH dehydrogenation can possibly help reserve natural resources while producing valuable chemicals. In this work, we will continue to explore the reaction pathway of EtOH dehydrogenation on NiCu SAAs.

CHAPTER 2

Methods

2.1   Density Functional Theory

The theoretical approach to this investigation was mainly focused on density function theory (DFT). The DFT calculations were carried out using Vienna ab initio Simulation Package (VASP) [20]. All the calculations were performed using the general gradient approximation (GGA) Perdew-Burke-Ernzerhof (PBE) functional [21]. The dDsC dispersion correction was employed to better describe van der Waals interactions [22]. A 3×3 unit cell of a 4-layer slab was modeled. The bottom 2 layers were fixed while the top 2 layers were allowed to relax throughout the optimization [9]. The Brillouin zones were sampled through a $5 \times 5 \times 1$ gamma k-point mesh. The core electrons were described by the projector-augmented wave (PAW) method [23, 24]. For the hydride formation modeling, a total vacuum of 24 Å was added to separate the slab from its periodic image in the z-direction. The electron kinetic cutoff energy was set at 450 eV. The convergence criteria for an electronic step and an ionic step were set to 10^{-7} eV and 0.01 eV/Å, respectively.

For the ethanol dehydrogenation simulation, the electron kinetic cutoff energy was set at 400 eV, and the convergence criteria for an electronic step and an ionic step were set to 10^{-6} eV and 0.02 eV/Å, respectively. The same functional and dispersion correction were used, and the same unit cell size was modeled. The same k-point mesh was used. All the calculations of adsorption on NiCu(111) were with spin polarizations [16]. The nudged elastic band (NEB) method was employed to find the transition state in each bond cleavage and hydrogen

migration step [25–27]. A total of 10 images including the initial and final images were generated for the NEB calculations. After performing the NEB calculation on each transition state, the image that was the highest in energy was taken to run a Dimer or quasi-Newton calculation until reaching convergence [28, 29]. In this study, all the initial and optimized structures were viewed using Atomic Simulation Environment (ASE) and visualization for Electronic and Structural Analysis (VESTA).

2.2 Lattice Parameter Optimization

In modeling the hydride formation in Pd/Au systems, to better match the Pd concentration of 20% under the experimental settings, a cubic cell of Au_3Pd_1 was created by placing one Pd atom at one corner of the cube and three Au atoms at the center of the three faces close to the Pd corner. The cubic cell is depicted in Figure 2.1. The Au_3Pd_1 cubic cell was then
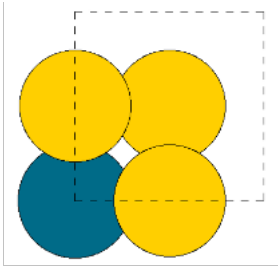
Figure 2.1: The cubic cell of Au_3Pd_1 alloy.

used as bulk for lattice constant optimization. The bulk chemical potentials were calculated for lattice constants from 4.00 Å to 4.20 Å with an increment of 0.02 Å. The data points were collected and then fitted into a quadratic polynomial, shown in Figure 2.2. The lattice constant value corresponding to the minimum chemical potential was then computed from the fitted quadratic polynomial, specifically, 4.09 Å. The fitted polynomial can be expressed in Equation 2.1.

$$y = 16.925x^2 - 138.54x + 266.93 \tag{2.1}$$
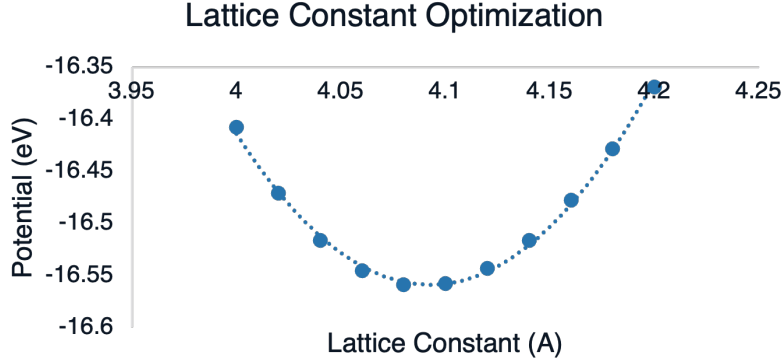
Figure 2.2: Lattice constant optimization for the Au_3Pd_1 alloy.

where y is the chemical potential (eV), and x is the lattice constant (Å).

The optimized lattice parameters of bulk Au and Pd using PBE functional are 3.93 Å and 4.14 Å, respectively. The expected lattice parameter for the Au_3Pd_1 was 4.08 Å. The expected value was computed from Vegard's Law, stating the lattice parameter of an alloy is the weighted average of each constituent's lattice parameter [30]. The expected lattice parameter of the Au_3Pd_1 alloy can be expressed in Equation 2.2. The optimized value from DFT calculations reached a very good agreement with the predicted value from Vegard's Law, with a percent error of less than 1%.

$$LC_{Au_3Pd_1} = \frac{1}{4}LC_{Pd} + \frac{3}{4}LC_{Au} \tag{2.2}$$

where $LC_{Au_3Pd_1}$, LC_{Pd}, and LC_{Au} are lattice constants of Au_3Pd_1 alloy, bulk Pd, and bulk Au, respectively.

The optimized alloy lattice was then employed in our calculations to obtain more accurate results. Two types of structures were generated for our studies, namely, monolayer

(1 ML) Pd structures and bilayer (2 ML) Pd structures, which incorporated 1 layer and 2 layers of Pd atoms on the top of Au layers, respectively. The side views of both structures are shown in Figure 2.3.
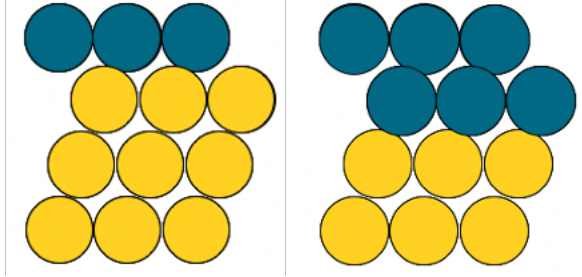

Figure 2.3: The side views of 1 ML and 2 ML Pd structures.

2.3 Free Energy of Formation Calculation

Two distinct schemes of electronic and free energy calculations were developed to better analyze the stabilization effect of the hydride formation in our structures. The two schemes employed different references and thus resulted in different units. The first scheme utilized the isolated subsurface Pd monomer and gaseous hydrogen molecule as references, and the corresponding unit was in eV. The equations for this scheme are shown below in Equations 2.3 and 2.4.

$$E_{form} = E_{hyd.sys} + (y-1)E_{slab} - yE_{Pd_1Au} - \frac{x}{2}E_{H_2} \tag{2.3}$$

$$G_{form} = E_{hyd.sys} + (y-1)E_{slab} - yE_{Pd_1Au} - \frac{x}{2}G_{H_2} \tag{2.4}$$

where E_{form} and G_{form} are electronic energy of formation and free energy of formation, $E_{hyd.sys}$ and $G_{hyd.sys}$ are electronic and free energy of the hydride structure, E_{H_2} and G_{H_2} electronic and free energy of the hydrogen molecule in the gas phase, E_{slab} is the electronic energy of the pure Au slab and E_{Pd_1Au} is the electronic energy of isolated Pd monomer in

9

the Au slab.

For the second scheme, the electronic and free energy values were normalized by the number of surface atoms in our model. Chemical potentials of bulk Au and alloy, the electronic energy of fixed Au slab with the same number of atoms, and electronic and free energies of the gaseous H_2 molecule under various conditions were used as references to compute normalized energies. The slab was separated into three parts, the top Pd region, the middle (non-bottom) Au region, and the bottom Au region, illustrated in Figure 2.4. Each region had n, m, and s atoms, respectively. The number of hydrogen atoms introduced in the system was x. Then, the electronic and free energy were computed using the equations below (Equations 2.5 and 2.6). The biggest advantage of using this approach is that the energy values were normalized and thus not dependent on the size of the unit cell.

Figure 2.4: The second scheme of free energy calculation.
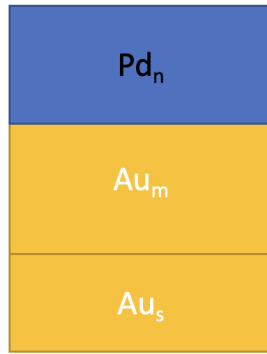
$$E_{form} = \frac{1}{s}(E_{hyd.sys} + (3n - m - s)\mu_{Au}) + \frac{1}{2s}(n + m + s)\mu_{Au} - \frac{1}{s}(n * \mu_{Au_3Pd_1} + \frac{x}{2}E_{H_2}) - \frac{1}{2s}E_{slab}$$
$$(2.5)$$

$$G_{form} = \frac{1}{s}(G_{hyd.sys} + (3n - m - s)\mu_{Au}) + \frac{1}{2s}(n + m + s)\mu_{Au} - \frac{1}{s}(n * \mu_{Au_3Pd_1} + \frac{x}{2}G_{H_2}) - \frac{1}{2s}E_{slab}$$
$$(2.6)$$

where E_{form} and G_{form} are electronic energy of formation and free energy of formation, $E_{hyd.sys}$ and $G_{hyd.sys}$ are electronic and free energy of the hydride structure, E_{H_2} and G_{H_2} electronic and free energy of the hydrogen molecule in the gas phase, E_{slab} is the electronic energy of the Au slab with all atoms fixed, μ_{Au} and $\mu_{Au_3Pd_1}$ are the chemical potentials of bulk Au and the Au_3Pd_1 alloy, and n, m, and s are demonstrated in Figure 2.4.

2.4 Carbon Monoxide (CO) Adsorption Correction

It was known that CO in the reaction environment could occupy the active sites and poison the catalyst surface [31]. However, DFT calculations could not precisely describe CO adsorption on catalytic metal surfaces, notably platinum (Pt) surfaces [32]. Generally, the CO molecule would overbind to the catalyst surface using the PBE functional. Thus, CO adsorption energy was corrected due to the inaccuracy by DFT. The method shown in Sumaria's work was used [33]. The CO adsorption energy (ΔE_{ads}) and the CO singlet-triplet excitation energy (ΔE_{S-T}) were computed using 5 different pseudopotentials. The ΔE_{ads} values were then plotted as a function of the ΔE_{S-T} values, and the ΔE_{S-T} was extrapolated to 6.095 eV to find the corrected ΔE_{ads} [33].

CHAPTER 3

Hydride Formation in Pd/Au Systems

3.1 Hydride Formation in 1 ML Pd Structures

For the 1 ML Pd structures, we first employed isolated subsurface Pd monomer as the reference to compute the energy of formation. As shown in Figures 3.1 and 3.2, the surface population of hydrogen atoms could help the structure reduce the energy of formation, yet the energy values remained positive, meaning that those structures are metastable. This also indicated that the stabilization effects did not offset the cost of forming the 1 ML Pd structure. Nevertheless, the stabilization effect caused by the adsorption of hydrogen atoms turned out to be promising as the electronic energy was decreased from 0.90 eV for the bare surface to 0.32 eV for the fully occupied surface. For this surface population, the hydrogen atoms were placed at the surface fcc sites, which resulted in the most stable structures. As we introduced more hydrogen atoms to the surface, they were separated as far apart as possible to fully use the Pd atoms in the surface layer and decrease the hydrogen repulsion effect.

The structure reached the full hydrogen coverage at the $x = 9$, where the H to Pd ratio is 1. An additional hydrogen atom was introduced to the surface layer beyond the full coverage to test if the extra hydrogen atom could continue to stabilize the system. The additional hydrogen atom was placed at one of the hcp sites while the original hydrogen atoms remained at the nine fcc sites. The top view is shown in Figure 3.3. The electronic energy tended to turn uphill beyond the full coverage.
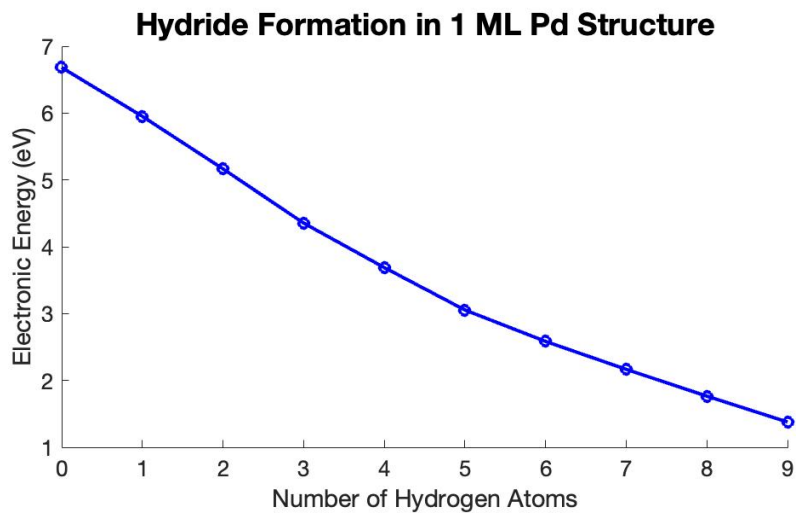
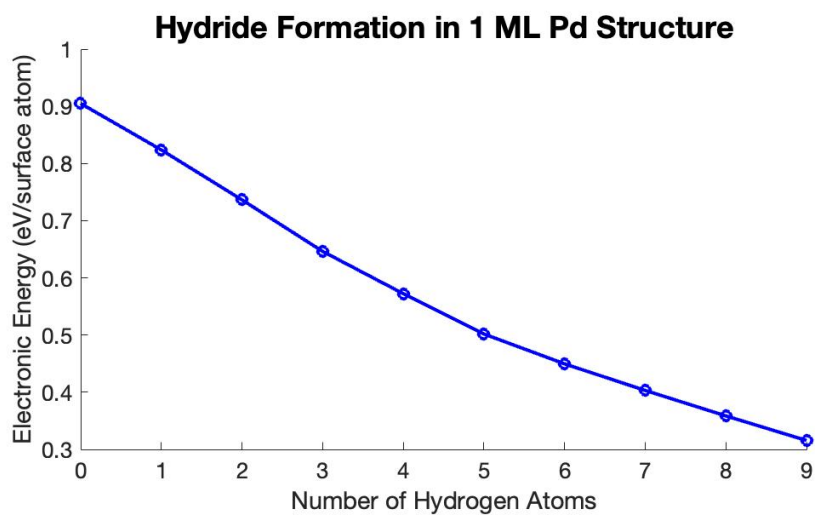Figure 3.1: The electronic energy of hydride formation in 1 ML Pd structures computed using Scheme 1.

Figure 3.2: The electronic energy of hydride formation in 1 ML Pd structures computed using Scheme 2.
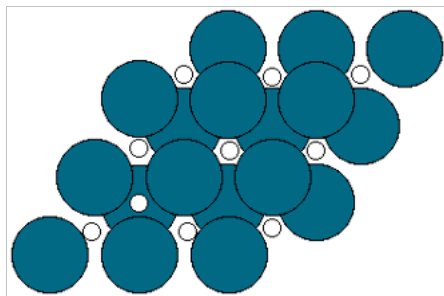
Figure 3.3: The top view of the 9 fcc + 1 hcp configuration.

For all calculations of 1 ML Pd structures, the contribution of vibrational entropy and zero-point energy was neglected. Because the number of hydrogen atoms in the 1 ML structures was not very significant, we did not carry out thorough vibrational frequency calculations. However, as the number of hydrogen atoms increased, we observed that the effect of vibration of each hydrogen atom built up and it could essentially play a role.

3.2 Hydride Formation in 2 ML Pd Structures

In the 1 ML Pd structures, we observed that the population of hydrogen atoms could stabilize the structure as discussed in Section 3.1. We were more interested to verify if the stabilization effect of hydrogen atoms was enhanced if more hydrogen atoms were introduced. Then, the 2 ML Pd structures were extensively studied for the hydride formation for the rest of this study since they have an extra layer of Pd atoms that could potentially accommodate more hydrogen atoms in the subsurface. For the subsurface population, we observed that the subsurface hydrogen atoms always favored the octahedral (oct) sites over the tetrahedral (tet) sites, and this observation matched with previous studies done by Hong et al [34].

We examined two possible options for the population of hydrogen atoms on the bare surface. The hydrogen atoms could go to either the surface fcc sites or the subsurface oct sites. DFT calculations proved that the hydrogen atoms which were initially introduced into the bare

14

surface preferred staying at the surface fcc sites to become lower in energy, shown in Figures 3.4 and 3.5, where the two different free energy calculation schemes were applied. The surface population of 2 ML Pd structures was downhill, similar to that of 1 ML Pd structures. DFT suggested there were no stable configurations formed for the subsurface population at lower hydrogen coverages, and the subsurface hydrogen atoms would divert to the surface sites. In these cases, the subsurface hydrogen atoms would go up to the surface layer to retain lower energy. Even at higher hydrogen content conditions, the subsurface-populated structures were far less stable than the surface-populated ones. This shows a good implication that in the case where the surface sites are not occupied, the hydrogen atoms will not diffuse to the subsurface until the surface reached full coverage. The vibrational entropy of each structure considered so far was considered negligible because the number of hydrogen atoms was reasonably small. Nonetheless, as the number of hydrogen atoms grew when populating the subsurface, this would not be the case, and the contribution of vibration could be significant.

It was reasonable to introduce additional hydrogen atoms to the subsurface after the surface layer was fully covered. At this point, the contributions of vibrational entropy and zero-point energy were not negligible as the effect of each individual hydrogen atom could possibly stack up. The vibrations were included in the free energy calculations for the structures with 9 or more hydrogen atoms. We compared the results with and without vibrations and observed a significant energy difference between the two free energy values. The difference in free energy for each structure at T $= 20\ ^oC$ and P $= 0.20$ atm is demonstrated in Figure 3.6. The calculations were computed using Scheme 2, and free energies were normalized by the number of surface atoms. Without considering the vibration, the most stable structure was 9 the fcc + 4 oct, starred in yellow. After adding the vibrational entropy and zero-point energy, the structure lowest in energy switched to the 9 hcp + 7 oct structure. Therefore, it was very possible that there was a discrepancy in the most stable structure after including the vibration, and it was essential to include the vibrational entropy and zero-point energy

15

for free energy calculations to ensure that we were able to find the actual structure that was the lowest in energy. The additional step to enhance the accuracy of the free energy calculations was to increase the k-point mesh. However, due to the high computational cost, especially for the highly hydrogen-populated structures, this study strictly kept the k-point mesh as aforementioned in Section 2.1.
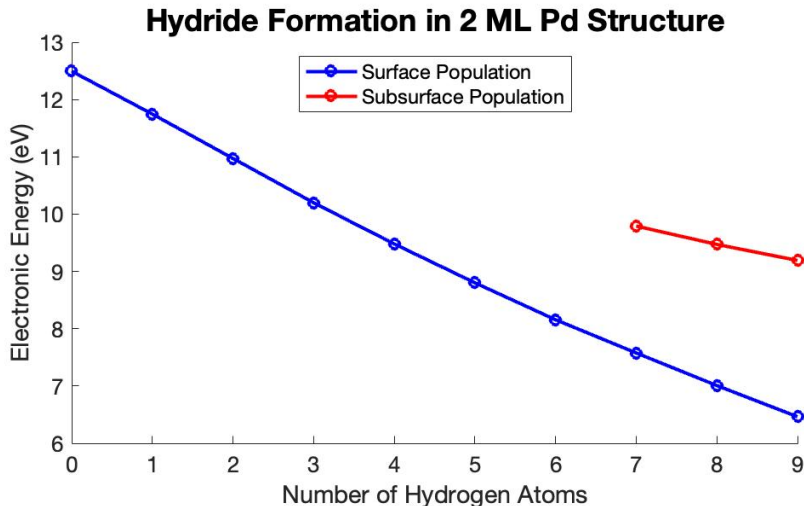

Figure 3.4: The electronic energy of hydride formation in 2 ML Pd structures using Scheme 1.

The trends of free energy of formation under the four experimental conditions were illustrated in Figure 3.7. All the calculations included the contribution of vibrational entropy and zero-point energy. We investigated four different conditions in total, two conditions at the low pressure (0.001 atm) and two conditions at the high pressure (0.20 atm). The low and medium temperatures (20 ^{o}C and 100 ^{o}C, respectively) were coupled with the low-pressure cases while the medium and high temperatures (100 ^{o}C and 210 ^{o}C, respectively) were coupled with the high-pressure cases. At 20 ^{o}C and 0.20 atm, the most stable was the 9 hcp + 7 oct structure, starred in green in the upper left panel of Figure 3.7. When the pressure was maintained at 0.20 atm and the temperature was increased to 100 ^{o}C, one subsurface
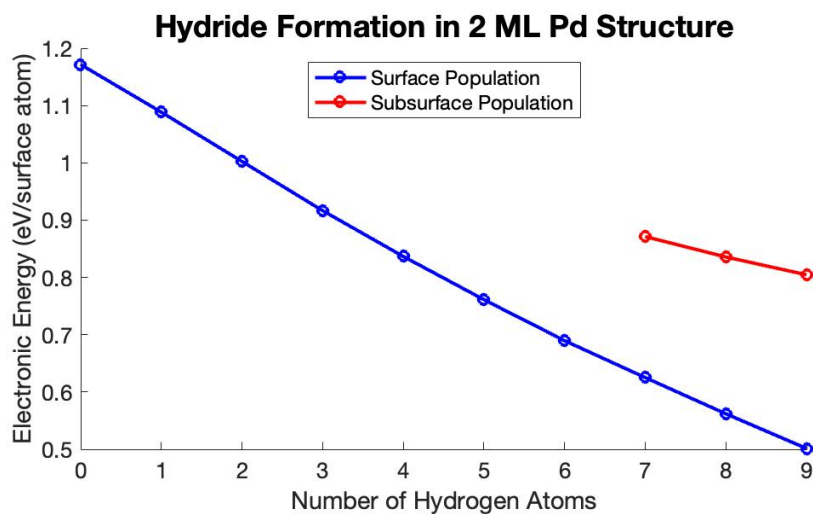
Hydride Formation in 2 ML Pd Structure

Figure 3.5: The electronic energy of hydride formation in 2 ML Pd structures using Scheme 2.

hydrogen atom desorbed, and the most stable became the 9 hcp + 6 oct structure shown in the upper right panel. When the temperature was kept constant and the pressure was decreased to 0.001 atm, all the remaining subsurface hydrogen atoms would desorb. The fully covered fcc structure with an empty subsurface was the lowest in energy, demonstrated in the lower left panel. In the case where the temperature was increased to 210 ^{o}C, the most stable structure remained, starred in green in the lower right panel. A brief summary was listed in Table 3.1. Low-pressure and high-temperature conditions did not favor the subsurface hydrogen population. We observed that part or all of the hydrogen atoms would desorb from the subsurface at an elevated temperature or a reduced pressure. At some points, the 9 fcc structure dominated with the lowest free energy, especially in the low-pressure regime. In the two high-pressure cases, the fcc and hcp structures were stabilized by the partially occupied subsurface before reaching their minima, and their energies turned uphill in the high subsurface content regime. On the other hand, in the two low-pressure cases, both the fcc and hcp structures did not gain any stabilization effect from the subsurface population, and the free energies of both structures were uphill from the low subsurface content regime

17

to the high subsurface content regime. For each case, a clear crossing occurred between the energies of fcc-covered and hcp-covered structures. In the lower subsurface hydrogen content regime, fcc structures were more favored while hcp structures were more preferred in the higher subsurface hydrogen regime.
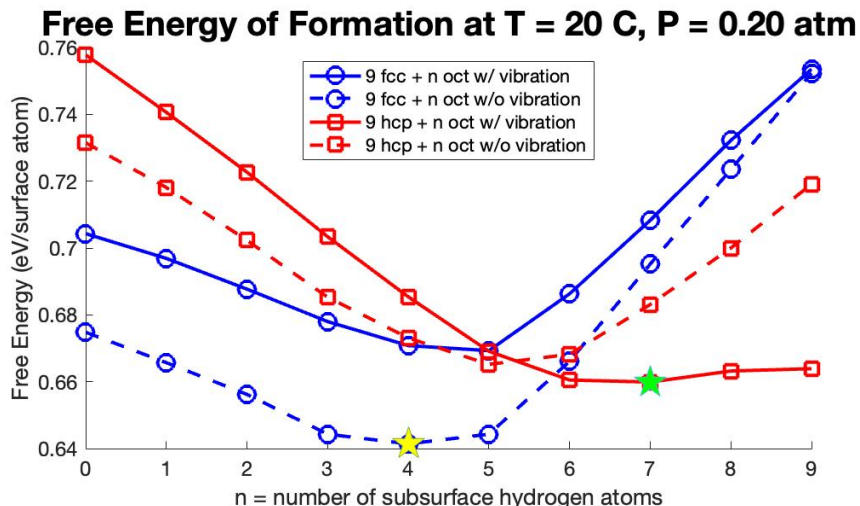

Figure 3.6: The contribution of vibration to the free energy under T = 20 ^{o}C and P = 0.20 atm.

Pressure (atm)	Temperature (^{o}C)	The Most Stable Structure	Free Energy (eV/surface atom)
0.001	100	9 fcc	0.8481
0.001	210	9 fcc	0.9553
0.20	20	9 hcp + 7 oct	0.6599
0.20	100	9 hcp + 6 oct	0.7539

Table 3.1: Summary of the most stable systems under different experimental conditions.

The most stable configurations for fcc and hcp 2 ML Pd structures at given hydrogen contents are shown below (Figures 3.8 and 3.9, respectively). The bottom 2 layers of Pd atoms

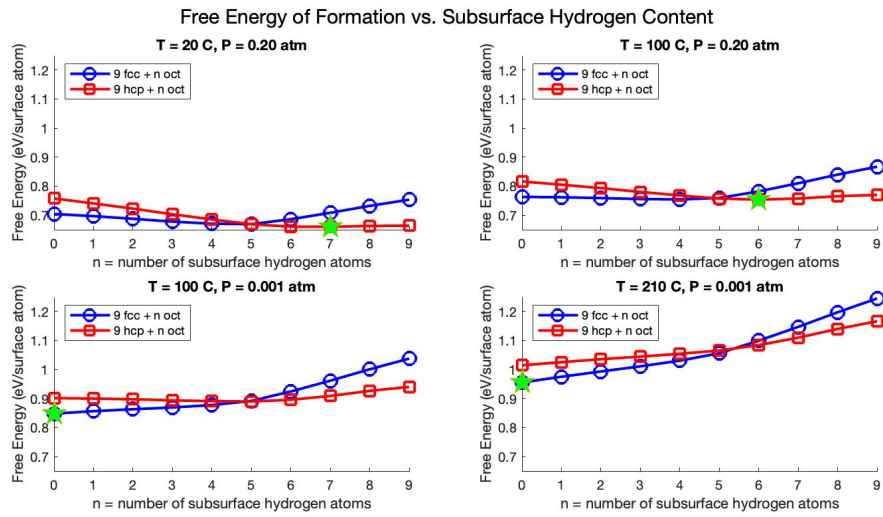Figure 3.7: The free energy of formation of 2 ML Pd structures under experimental conditions.

are removed for illustration purposes. The green hydrogen atoms indicate the locations of subsurface hydrogen atoms, and the pink hydrogen atoms represent the subsurface hydrogen atoms.
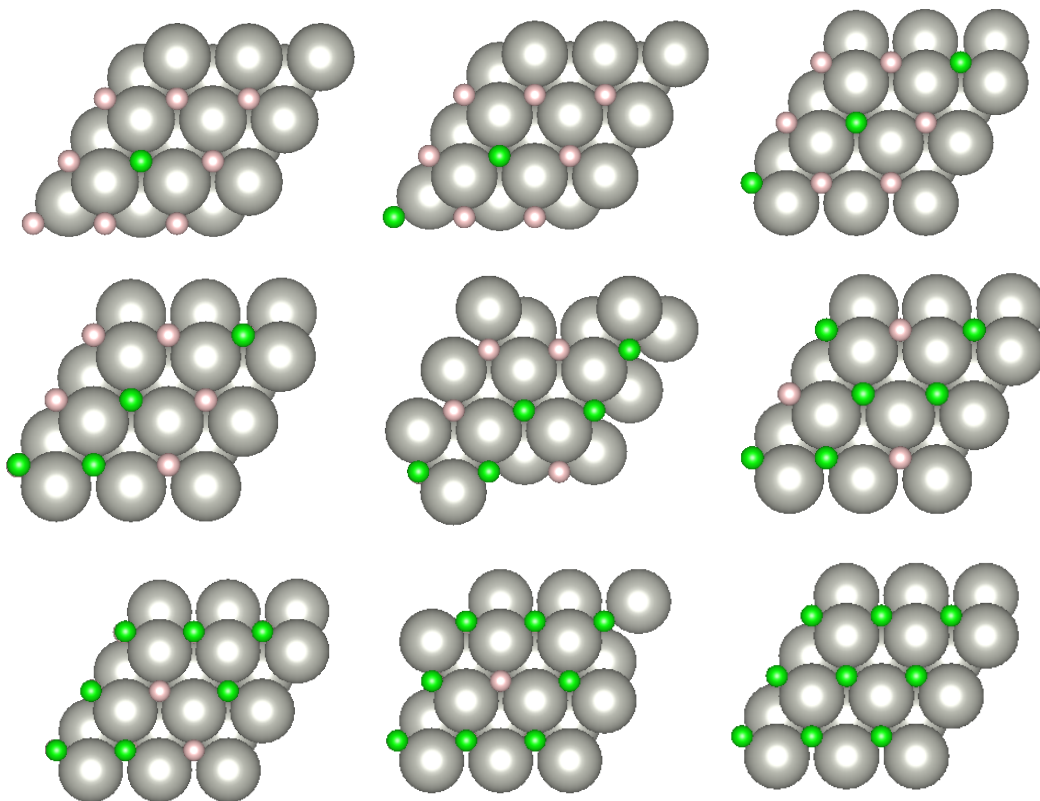
Figure 3.8: The most stable fcc configurations for the 2ML Pd structures.
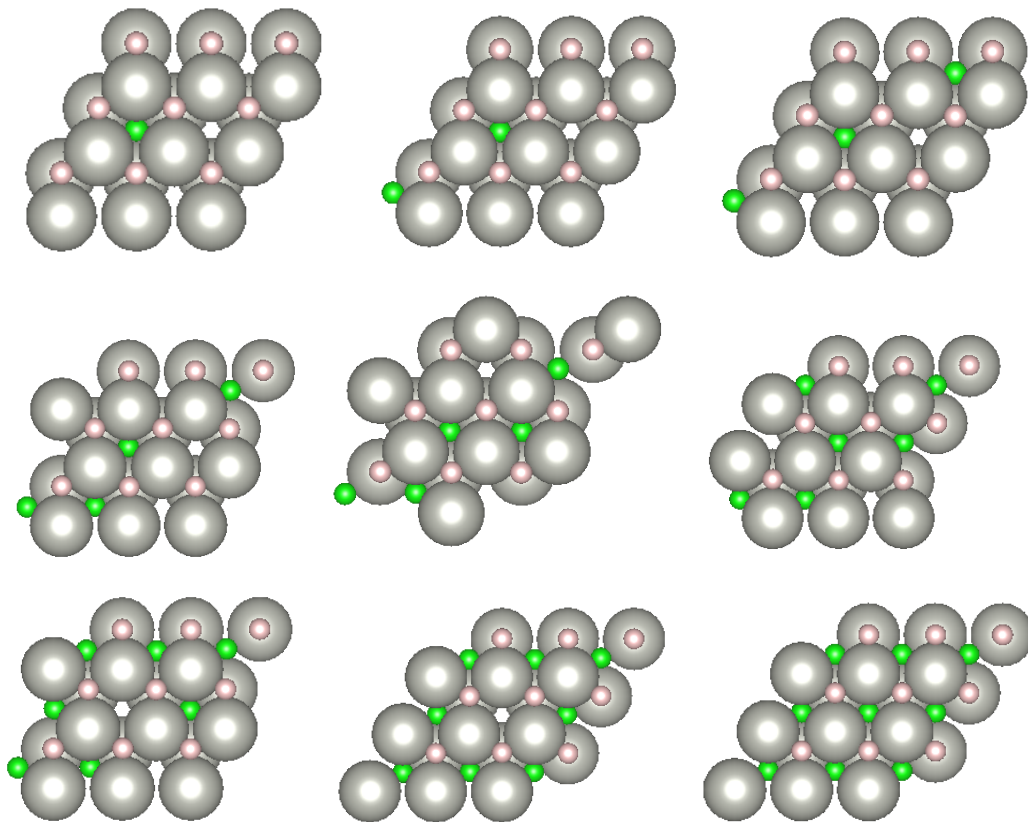
Figure 3.9: The most stable hcp configurations for the 2ML Pd structures.

3.3   Summary

In this work, we carried out a thorough computational investigation of the hydride formation in the PdAu systems, namely monolayer (1 ML) and bilayer (2 ML) Pd structures. We observed that the hydride formation in both systems was not favorable, and the geometry-optimized structures were thus metastable. Nonetheless, the structures were drastically stabilized by introducing hydrogen atoms into the systems. The DFT calculations also revealed the preferred sites for both surface and subsurface hydrogen atoms under different coverage regimes.

CHAPTER 4

Ethanol Dehydrogenation on the Ni$_2$Cu(111) Surface

4.1 Mechanistic Investigation of Ethanol Dehydrogentaion

On the Ni$_2$Cu surface, the dehydrogenation reaction would go through an O-H bond cleavage, followed by a C-H bond cleavage, to form acetaldehyde and hydrogen as final products. This was shown as a preferred pathway in the previous work by Patel et al [16]. The same sequence of bond breaking was also predicted by scaling relations. The electronic energy profile of this reaction was presented in Figure 4.1. The overall reaction can be written below.

$$CH_3CH_2OH \longrightarrow CH_2CHO + H_2$$
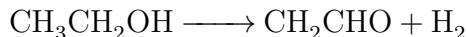
The initial state (IS) was the clean Ni$_2$Cu surface with the gaseous EtOH. The following state (State I) was the EtOH adsorption on the surface, resulting in 0.61 eV lower in electronic energy. The O-H bond cleavage occurred through the first transition state (TS-I). The overall barrier for the O-H bond cleavage step was 0.84 eV. The resultant intermediates (State II) were the ethoxy radical and hydrogen atom. The relative free energy of State II was 0.96 eV lower compared to the initial state. The hydrogen atom from the O-H bond breaking was removed (State III), and the ethoxy radical was rearranged to the hcp site (State IV) in between the two Ni atoms before the second bond-breaking process. The purpose of this rearrangement of the ethoxy radical was to fully utilize the two Ni atoms in the following C-H bond cleavage. The rearrangement was assumed to be barrierless. The rearranged ethoxy
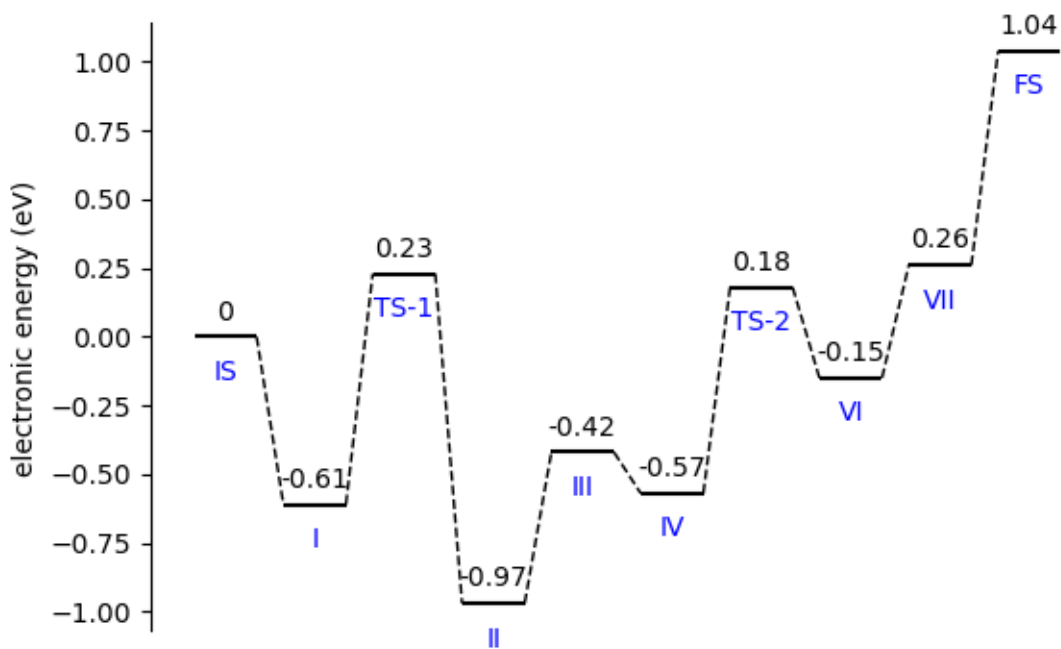
Figure 4.1: The electronic energy profile of the EtOH dehydrogenation reaction on the Ni$_2$Cu(111) Surface.

radical went through the second transition state (TS-II) to break the C-H bond. This bond cleavage process had an overall 0.75 eV barrier. Again, the hydrogen atom that was produced from the bond-breaking step was removed (State VII). Then the acetaldehyde would desorb from the catalyst surface. The final state (FS) would be the clean Ni_2Cu surface and the gaseous acetaldehyde. The top and side views of each state are shown below (Figure 4.2). The pink, red, orange, grey, and brown atoms are hydrogen, oxygen, copper, nickel, and carbon, respectively.

Figure 4.2: The top and side views of major states (I, TS-1, II, III, IV, TS-2, VI, and VII, respectively) in the EtOH dehydrogenation reaction.

4.2 CO Adsorption on the Ni$_2$Cu(111) Surface
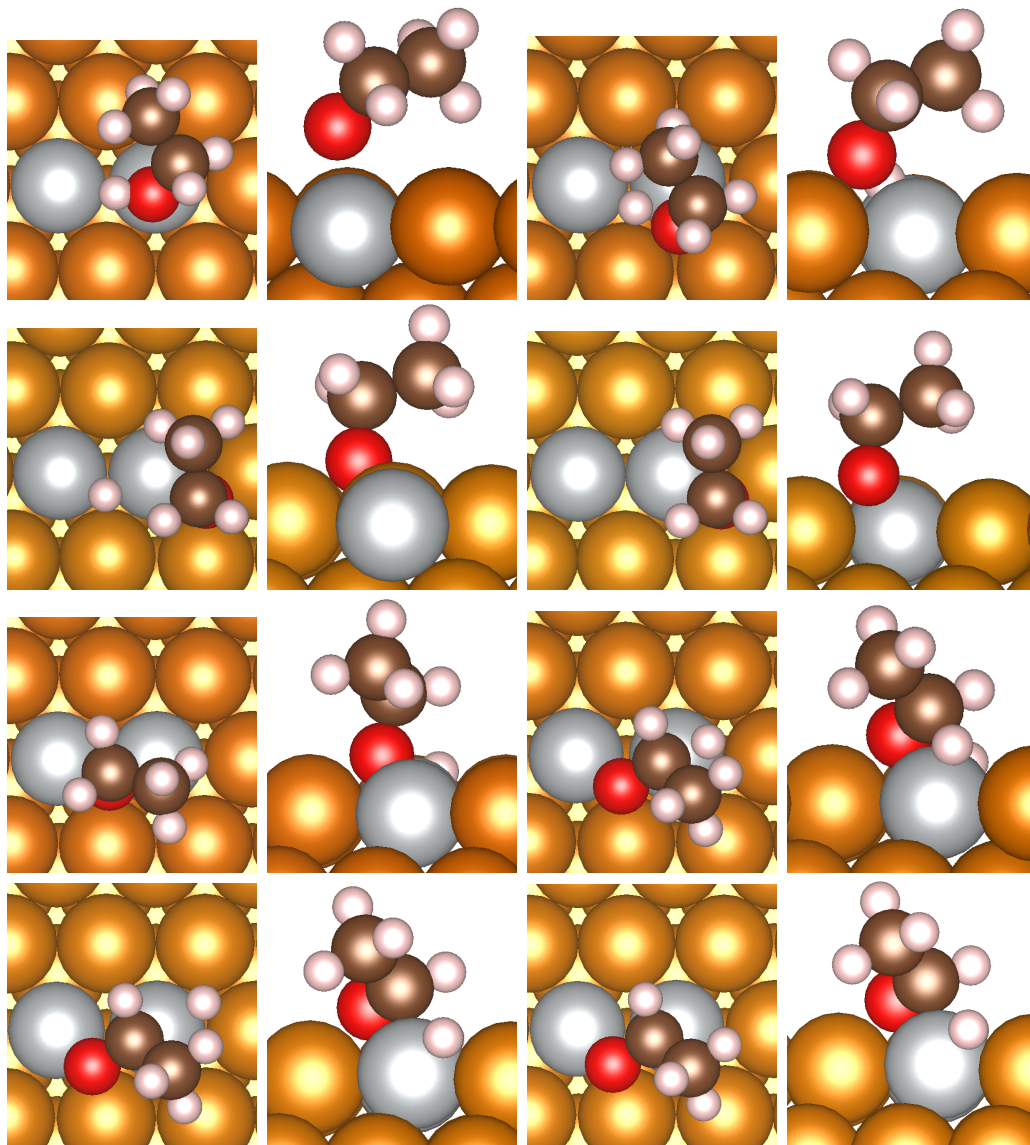
The CO adsorption energies on top and bridge sites computed using 5 different pseudopo-
tentials were presented in Table 4.1. Top, fcc, hcp, and bridge adsorption modes were
investigated, but fcc and hcp adsorption modes diverted to the bridge adsorption mode after
the geometry optimization, and the resultant adsorption energies were very similar to that
of the bridge mode. Therefore, fcc, hcp, and bridge adsorption modes were considered as one
unique mode. After applying the correction, the adsorption energies of CO on the top and
bridge sites were determined to be -1.54 eV, and -1.66 eV, respectively. Not surprisingly, the
most stable adsorption mode after the correction was the bridge site adsorption because the
CO molecule at the bridge site could potentially benefit from both Ni atoms on the surface.
The CO adsorption modes studied in this work included fcc, hcp, bridge, and top sites. The
configuration of each mode is shown in Figure 4.3. The atoms in orange, grey, red, and brown
are copper, nickel, oxygen, and carbon atoms, respectively, and only the top two layers were
shown. The figure only demonstrated the configurations using the n pseudopotentials, but
other pseudopotentials yield extremely similar results.

Pseudopotential	ΔE_{S-T} (eV)	$\Delta E_{ads,top}$ (eV)	$\Delta E_{ads,bridge}$ (eV)
GW	5.59	-1.73	-1.96
GW_new	5.63	-1.73	-1.95
s	5.25	-1.86	-2.18
h	5.64	-1.72	-1.94
n	5.56	-1.74	-1.98

Table 4.1: Summary of ΔE_{S-T} and ΔE_{ads} on top and bridge sites using different pseudopo-
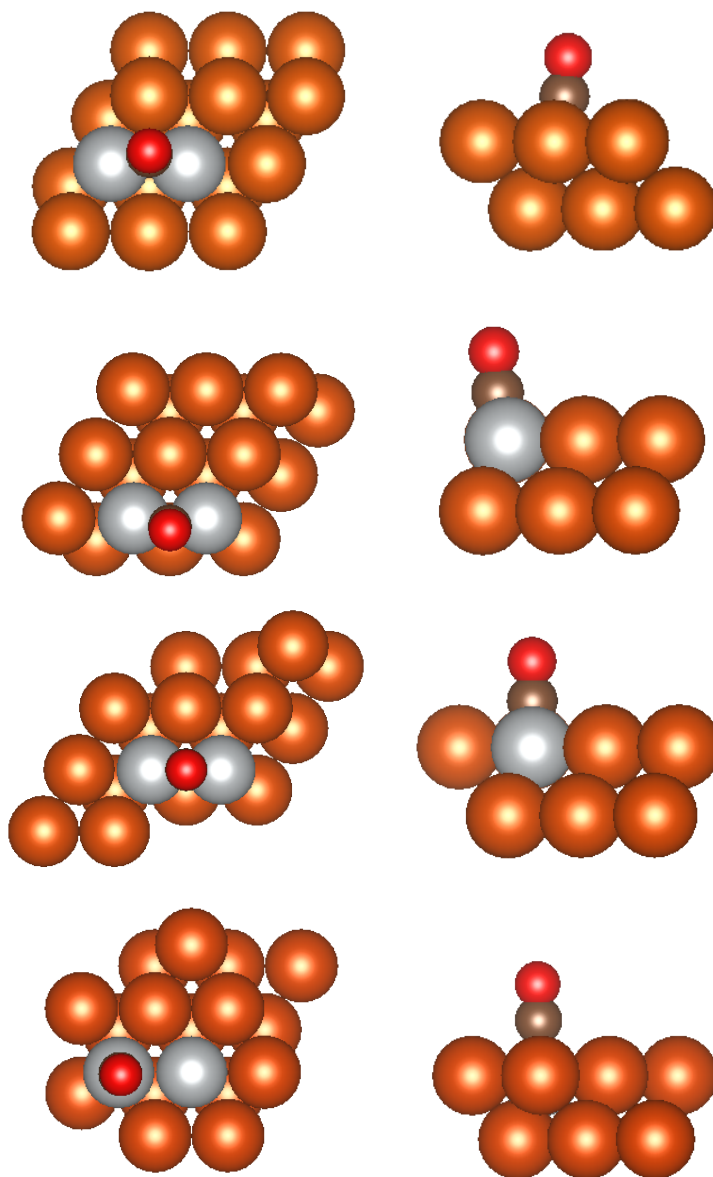tentials.

Figure 4.3: The CO adsorption modes on the $Ni_2Cu(111)$ surface, fcc, hcp, bridge, and top modes, respectively.
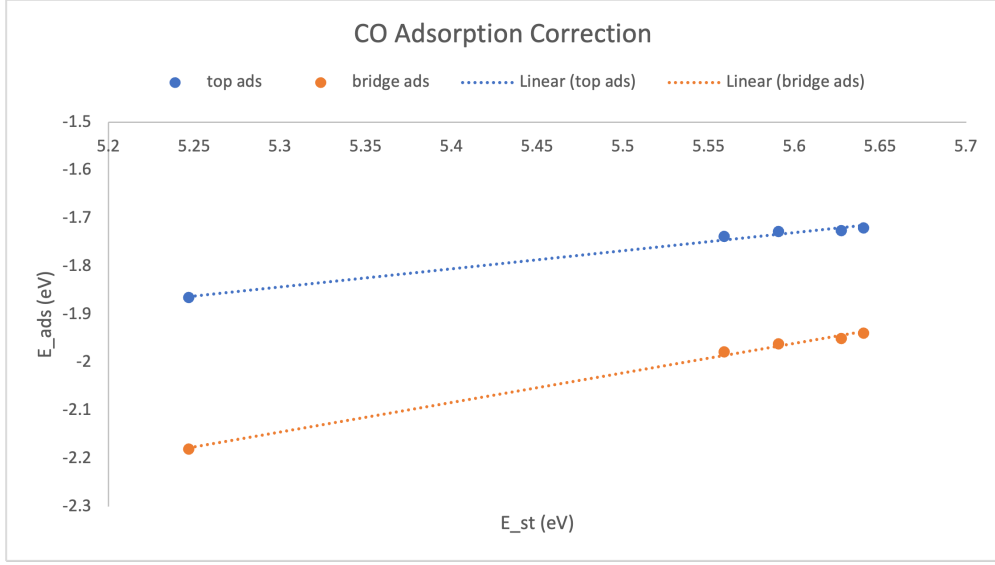
Figure 4.4: The linear extrapolation for CO adsorption energy correction.

The linear extrapolations of the top and bridge adsorption modes are shown in Figure 4.4. The blue and red data points represent the top and bridge adsorption of CO on the Ni$_2$Cu(111) surface, respectively. The blue and red dotted lines are the corresponding linear extrapolations, shown in Equations 4.1 and 4.2.

$$E_{ads} = 0.3763\Delta E_{S-T} - 3.8369 \tag{4.1}$$

$$E_{ads} = 0.6163\Delta E_{S-T} - 5.4116 \tag{4.2}$$

where ΔE_{S-T} and E_{ads} are the CO singlet-triplet excitation energy and the CO adsorption energy, respectively.

After applying the correction, the adsorption energies of CO on the top and bridge sites were determined to be -1.54 eV, and -1.66 eV, respectively. Not surprisingly, the most stable adsorption mode after the correction was the bridge site adsorption because the CO molecule at the bridge site could potentially benefit from both Ni atoms on the surface. Compared

to the adsorption of EtOH discussed in the previous section, the CO adsorption energy was more negative, indicating the binding of CO molecules was stronger.

4.3 Summary

In this work, we performed a mechanistic exploration of the EtOH dehydrogenation reaction on the Ni$_2$Cu(111) surface. We also implemented a correction on the CO adsorption on the catalyst surface. The overall reaction was expected to go through an O-H bond cleavage, followed by a C-H bond cleavage, suggested by the DFT calculations. The first O-H bond breaking step was the rate-limiting step for the overall reaction.

CHAPTER 5

Conclusion

Hydride formation is found very common in Pd ensembles. The free energies of formation of hydride structures of monolayer (1ML) Pd and bilayer (2ML) Pd structures were investigated by DFT calculations. The study used PBE functional with dDsC correction for Van der Waals interactions. In the 1ML Pd structures, surface hydrogen atoms were found to prefer the fcc sites, which results in lower energy, thus a more stable configuration. The spatial separation of hydrogen atoms also helped mitigate the lateral repulsion and therefore reduce the energy of formation slightly. The structures were more stabilized as the number of hydrogen atoms grew. However, the stabilization effects cannot offset the overall cost of the formation of the monolayer of Pd atoms. Therefore, these structures were considered metastable.

In the 2 ML Pd structures, the direct population of subsurface sites was not favored. There were no stable configurations found under low hydrogen contents, and the configurations found under high hydrogen contents were much less stable than the surface-populated ones. Besides, in the 2 ML Pd structures, subsurface hydrogen atoms were found to prefer the oct sites while surface hydrogen atoms were found to favor the fcc sites under low subsurface hydrogen contents and hcp sites under high subsurface hydrogen contents. Vibrational entropy and zero-point energy were shown to play an essential role in computing the free energy of formation. Overall, the 2ML Pd structures that were studied were also metastable, but the introduction of an additional layer of hydrogen atoms continued to bring down the free energy. It is also important to note that high-temperature and low-pressure conditions

will not favor the subsurface hydrogen population. Under these conditions, the subsurface hydrogen atoms will fully or partially desorb to retain the lowest energy.

For the EtOH dehydrogenation reaction on the $Ni_2Cu(111)$ surface, the O-H bond scission would occur first, followed by the C-H bond cleavage. The configurations of transition states were determined using the climbing nudged elastic band (NEB), dimer, and quasi-Newton methods. The reaction was controlled by the O-H bond cleavage process, with an overall barrier of 1.00 eV. The calculation value reached a good agreement with the predicted value from the scaling relation. The overall reaction involved rearrangements of intermediates. By carefully tuning the initial or final states of the bond scission process, the process could go through a transition state that is lower in energy. The Ni_2Cu surface tends to be more promising in EtOH dehydrogenation reactions compared to the NiCu surface, with 0.18 eV lower in the overall reaction barrier [18]. For future works, temperature-programmed desorption (TPD) and microkinetic modeling (MKM) should be carried out to extract more insights from reaction kinetics [35, 36].

Bibliography

[1] J. C. Védrine in *Metal Oxides in Heterogeneous Catalysis*, Metal Oxides, Elsevier, **2018**, pp. 551–569.

[2] C. Leyva, M. S. Rana, F. Trejo, J. Ancheyta, *Industrial & Engineering Chemistry Research* **2007**, *46*, 7448–7466.

[3] T. F. Degnan, *Topics in Catalysis* **2000**, *13*, 349–356.

[4] H. Liu, *Chinese Journal of Catalysis* **2014**, *35*, 1619–1640.

[5] T. Zurrer, K. Wong, J. Horlyck, E. C. Lovell, J. Wright, N. M. Bedford, Z. Han, K. Liang, J. Scott, R. Amal, *Advanced Functional Materials* **2021**, *31*, 2007624.

[6] B. W. J. Chen, L. Xu, M. Mavrikakis, *Chemical Reviews* **2021**, *121*, 1007–1048.

[7] K. Lévay, K. D. Tóth, T. Kárpáti, L. Hegedűs, *ACS Omega* **2020**, *5*, 5487–5497.

[8] L. L. Jewell, B. H. Davis, *Applied Catalysis A: General* **2006**, *310*, 1–15.

[9] T. P. Senftle, M. J. Janik, A. C. T. van Duin, *The Journal of Physical Chemistry C* **2014**, *118*, 4967–4981.

[10] H. M. Luong, M. T. Pham, T. Guin, R. P. Madhogaria, M.-H. Phan, G. K. Larsen, T. D. Nguyen, *Nature Communications* **2021**, *12*, 2414.

[11] R. T. Hannagan, G. Giannakakis, R. Réocreux, J. Schumann, J. Finzel, Y. Wang, A. Michaelides, P. Deshlahra, P. Christopher, M. Flytzani-Stephanopoulos, M. Stamatakis, E. C. H. Sykes, *Science* **2021**, *372*, 1444–1447.

[12] F.-W. Chang, H.-C. Yang, L. S. Roselin, W.-Y. Kuo, *Applied Catalysis A: General* **2006**, *304*, 30–39.

[13] W.-H. Lin, H.-F. Chang, *Catalysis Today* **2004**, *97*, 181–188.

[14] G. Giannakakis, P. Kress, K. Duanmu, H. T. Ngan, G. Yan, A. S. Hoffman, Z. Qi, A. Trimpalis, L. Annamalai, M. Ouyang, J. Liu, N. Eagan, J. Biener, D. Sokaras, M. Flytzani-Stephanopoulos, S. R. Bare, P. Sautet, E. C. H. Sykes, *Journal of the American Chemical Society* **2021**, *143*, 21567–21579.

[15] J. Shan, J. Liu, M. Li, S. Lustig, S. Lee, M. Flytzani-Stephanopoulos, *Applied Catalysis B: Environmental* **2018**, *226*, 534–543.

[16] D. A. Patel, G. Giannakakis, G. Yan, H. T. Ngan, P. Yu, R. T. Hannagan, P. L. Kress, J. Shan, P. Deshlahra, P. Sautet, E. C. H. Sykes, *ACS Catalysis* **2023**, *13*, 4290–4303.

[17] K. G. Papanikolaou, M. Stamatakis, *Catalysis Science & Technology* **2021**, *11*, 3681–3696.

[18] E. J. Evans, H. Li, W.-Y. Yu, G. M. Mullen, G. Henkelman, C. B. Mullins, *Phys. Chem. Chem. Phys.* **2017**, *19*, 30578–30589.

[19] Z.-T. Wang, R. A. Hoyt, M. El-Soda, R. J. Madix, E. Kaxiras, E. C. H. Sykes, *Topics in Catalysis* **2018**, *61*, 328–335.

[20] G. Kresse, J. Furthmüller, *Computational Materials Science* **1996**, *6*, 15–50.

[21] J. P. Perdew, K. Burke, M. Ernzerhof, *Phys. Rev. Lett.* **1996**, *77*, 3865–3868.

[22] S. N. Steinmann, C. Corminboeuf, *Journal of Chemical Theory and Computation* **2011**, *7*, 3567–3577.

[23] P. E. Blöchl, *Phys. Rev. B* **1994**, *50*, 17953–17979.

[24] G. Kresse, D. Joubert, *Phys. Rev. B* **1999**, *59*, 1758–1775.

[25] G. Henkelman, B. P. Uberuaga, H. Jónsson, *The Journal of Chemical Physics* **2000**, *113*, 9901–9904.

[26] H. JÓNSSON, G. MILLS, K. W. JACOBSEN, *Classical and Quantum Dynamics in Condensed Phase Simulations* **1998**, DOI 10.1142/9789812839664_0016.

[27] G. Henkelman, H. Jónsson, *The Journal of Chemical Physics* **2000**, *113*, 9978–9985.

[28] G. Henkelman, H. Jónsson, *The Journal of Chemical Physics* **1999**, *111*, 7010–7022.

[29] C. Freysoldt, *Computational Materials Science* **2017**, *133*, 71–81.

[30] K. T. Jacob, S. Raj, L. Rannesh, *International Journal of Materials Research* **2007**, *98*, 776–779.

[31] D. A. Patel, R. T. Hannagan, P. L. Kress, A. C. Schilling, V. Çınar, E. C. H. Sykes, *The Journal of Physical Chemistry C* **2019**, *123*, 28142–28147.

[32] L. K. G, I. Kundappaden, R. Chatanathodi, *Surface Science* **2019**, *681*, 143–148.

[33] V. Sumaria, L. Nguyen, F. F. Tao, P. Sautet, *ACS Catalysis* **2020**, *10*, 9533–9544.

[34] J. Hong, J.-H. Bae, H. Jo, H.-Y. Park, S. Lee, S. J. Hong, H. Chun, M. K. Cho, J. Kim, J. Kim, Y. Son, H. Jin, J.-Y. Suh, S.-C. Kim, H.-K. Roh, K. H. Lee, H.-S. Kim, K. Y. Chung, C. W. Yoon, K. Lee, S. H. Kim, J.-P. Ahn, H. Baik, G. H. Kim, B. Han, S. Jin, T. Hyeon, J. Park, C. Y. Son, Y. Yang, Y.-S. Lee, S. J. Yoo, D. W. Chun, *Nature* **2022**, *603*, 631–636.

[35] J. L. Falconer, J. A. Schwarz, *Catalysis Reviews* **1983**, *25*, 141–227.

[36] P. Stoltze, *Progress in Surface Science* **2000**, *65*, 65–150.